Biomaterials 288 (2022) 121741

Contents lists available at ScienceDirect

Biomaterials

journal homepage: www.elsevier.com/locate/biomaterials

High-efficient engineering of osteo-callus organoids for rapid bone regeneration within one month

Chang Xie [a,b,c,1], Renjie Liang [a,b,c,1], Jinchun Ye [a,b,c,1], Zhi Peng [a,b,c], Heng Sun [a,b,c], Qiuwen Zhu [a,b,c], Xilin Shen [a,b,c], Yi Hong [a,b,c], Hongwei Wu [a,b,c], Wei Sun [a,b,c], Xudong Yao [a,e], Jiajin Li [a,b,c], Shufang Zhang [a,b,c], Xianzhu Zhang [a,b,c,**], Hongwei Ouyang [a,b,c,d,*]

[a] Dr. Li Dak Sum & Yip Yio Chin Center for Stem Cells and Regenerative Medicine, and Department of Orthopedic Surgery of the Second Affiliated Hospital, Zhejiang University School of Medicine, Hangzhou, China
[b] Department of Sports Medicine, Zhejiang University School of Medicine, Hangzhou, China
[c] Zhejiang University-University of Edinburgh Institute, Zhejiang University School of Medicine, and Key Laboratory of Tissue Engineering and Regenerative Medicine of Zhejiang Province, Zhejiang University School of Medicine, Hangzhou, China
[d] China Orthopedic Regenerative Medicine Group (CORMed), Hangzhou, China
[e] The Fourth Affiliated Hospital, Zhejiang University School of Medicine, Yiwu, China

ARTICLE INFO

Keywords:
3D cell culture system
Bioprinting
Organoids
Endochondral ossification
Bone regeneration

ABSTRACT

Large bone defects that cannot form a callus tissue are often faced with long-time recovery. Developmental engineering-based strategies with mesenchymal stem cell (MSC) aggregates have shown enhanced potential for bone regeneration. However, MSC aggregates are different from the physiological callus tissues, which limited the further endogenous osteogenesis. This study aims to achieve engineering of osteo-callus organoids for rapid bone regeneration in cooperation with bone marrow-derived stem cell (BMSC)-loaded hydrogel microspheres (MSs) by digital light-processing (DLP) printing technology and stepwise-induction. The printed MSC-loaded MSs aggregated into osteo-callus organoids after chondrogenic induction and showed much higher chondrogenic efficiency than that of traditional MSC pellets. Moreover, the osteo-callus organoids exhibited stage-specific gene expression pattern that recapitulated endochondral ossification process, as well as a synchronized state of cell proliferation and differentiation, which highly resembled the diverse cell compositions and behaviors of developmentally endochondral ossification. Lastly, the osteo-callus organoids efficiently led to rapid bone regeneration within only 4 weeks in a large bone defect in rabbits which need 2–3 months in previous tissue engineering studies. The findings suggested that *in vitro* engineering of osteo-callus organoids with developmentally osteogenic properties is a promising strategy for rapid bone defect regeneration and recovery.

1. Introduction

Bone injury is one of the most common traumas in skeletal tissues, causing serious socio-economic burdens. Unlike regular injuries, large bone defects at critical size that cannot form a callus tissue are often faced with limited self-healing capability and long-time recovery, which may eventually lead to uncomplete regeneration or injury non-union. Generally, large bone defects especially critical-sized defects can hardly achieve complete regeneration within 3 months [1–4]. Current clinical strategies for large bone defect repair mainly include the implantation of metallic devices, autografts, allografts and artificial grafts. However, these treatments have their drawbacks, such as the secondary damage due to the removal of the metallic devices, damage and restricted volume of donor site when applying autografts. In addition, there are also high risks of disease transmission of allografts and poor osteointegration between artificial grafts and the host tissues. Besides,

* Corresponding author. School of Basic Medical Sciences, and Department of Orthopedic Surgery of the Second Affiliated Hospital, Zhejiang University School of Medicine, Hangzhou, Zhejiang, China.
** Corresponding author. School of Basic Medical Sciences, and Department of Orthopedic Surgery of the Second Affiliated Hospital, Zhejiang University School of Medicine, Hangzhou, Zhejiang, China.
E-mail addresses: 11518129@zju.edu.cn (X. Zhang), hwoy@zju.edu.cn (H. Ouyang).
[1] These authors contributed equally to this work.

https://doi.org/10.1016/j.biomaterials.2022.121741
Received 11 January 2022; Received in revised form 19 July 2022; Accepted 9 August 2022
Available online 19 August 2022

none of these strategies could significantly reduce the healing time of large bone defects. Therefore, these limitations have urged more efficient strategies for enhanced bone regeneration.

To mimic native healing processes and guarantee predictive *in vivo* bone regeneration performance, the concept of "developmental engineering" was proposed to mimic key developmental events during endochondral ossification [5], which is the mechanism responsible for the development and regeneration of major bone tissues, including all long bones and appendicular skeleton [6,7], and guide the design of biomimetic constructs. For bone regeneration, cell aggregation and condensation are the initial processes in endochondral ossification. Stem cell aggregates-based strategies have emerged as potential options of developmental engineering for their mimicking a more physiological microenvironment and their unique self-organization potential [8–10]. Recent studies recapitulating stem cell condensation by pure cell aggregates such as stem cell spheroids [11] and stem cell sheets [12], have been demonstrated to promote ectopic or in situ bone formation at a certain degree. However, such strategies simply achieved stem cell aggregation and few of them recapitulated the further differentiation and maturation processes during endochondral ossification, which is not consistent with the formation of ossification center or the progression of native callus tissue.

The formation of native callus tissue is highly independent on a series of successive processes. During the activated endochondral ossification of bone injury repair, resident mesenchymal stem cells actively condensate and differentiate to form a cartilage template called "callus" in the defect sites, followed by hypertrophy, calcification and apoptosis, as well as the subsequent recruitment and osteogenic differentiation of local stem cells [13]. These processes indicate the multiple-phases and multicellular scenario are required when bioengineering a callus-mimicking construct for efficient bone regeneration. Therefore, the multicellular composition and transcriptomic similarity between the engineered constructs and native bone callus tissue are considered as more biomimetic strategies, which are also in an urgent need for the fabrication of callus-like transplants.

Organoid-based strategies have been proposed to highly recapitulate the functional characteristics of native organs [14–16], which provide potential strategies for callus-organoid construction and efficient bone regeneration. Researches have established organoids in nervous system [15], urinary system [16] and digestive system [17] to understand their development and disease by 3D cell assemblies. However, the pure cell aggregates-based organoids are accompanied by limitations on the requirement of a large number of cells when applied in large-sized defect regeneration. Nutrient shortage and possible cell necrosis in the central regions of macro-sized cell aggregates remain a problem to be solved [18], which would lead to inhomogeneous tissue regeneration and even repair failure especially for bone defect repair. Besides, mass production of constructed organoid units for large defects still remains a challenge. 3D bioprinting has been widely used in regenerative medicine to control the spatial deposition of printed cells and produce constructs with native cellular composition and tissue structures. Recently, more researches focused on the construction of hydrogel-based organoids by 3D printing technology with controllable size and structure, as well as mass production of constructed organoids with high cell viability [19–21]. The combination of organoids conception and 3D bioprinting provides a considerable potential option for fabrication of callus-like organoids.

Microsphere (MS)-based cell culture system has been reported as a platform for stem cell condensation and expansion [22,23], chondrogenic and osteogenic differentiation [24–27] and bottom-up tissue engineering strategies [4,28], which exactly fulfils the cellular requirements for the construction of callus-like organoids *in vitro*. More importantly, MS-based culture system avoids possible nutrient shortage and cell necrosis in the central regions of pure cell aggregates. Our previous study has shown that DLP (digital light processing) technique, a layer-by-layer 3D printing technology, has provided an optimized solution for scale-up fabrication of uniform hydrogel MSs with high cell viability and desired size [29]. Gelatin methacrylate (GelMA) contains abundant sequences of arginine-glycine-aspartic acid (RGD) and the target sequences of matrix metalloproteinase (MMP), which resembles to native extracellular matrix (ECM) of collagen-rich tissue and can be applied for organoids printing [30]. Provided with extensive cell attachment surface and relative soft matrix, the MS-based system is advantageous for *in vitro* stem cell culture with stable cell viability and stem cell phenotype [29], which implies the potential and availability of MS-based callus organoids for critical-sized bone repair.

In this work, we presented a cell-saving strategy with scalable production of bone marrow-derived stem cells (BMSCs)-encapsulated osteo-callus organoids by DLP-based bioprinting technique. Herein, *in vitro* mesenchymal condensation by natural aggregation of these BMSC-loaded MS units was subsequently induced in chondrogenic medium for 3 weeks into developmental osteo-callus organoids. The phenotypic gene expression pattern of the osteo-callus organoids during the gradual maturation *in vitro* was investigated compared with that in native endochondral ossification. Furthermore, the osteo-callus organoids were implanted *in vivo* to investigate ectopic bone formation and in-situ bone regeneration ability, respectively. The osteo-callus organoids acting as microniches led to efficient ectopic bone formation and contributed to rapid in situ bone regeneration within 4 weeks in large bone defect. In both cases, new bone formation under the implantation of osteo-callus organoids exhibited a temporal-forward healing phase which stepped over the chondrogenesis. Our study introduces the biomimetic osteo-callus organoids can act as microniches that mimic callus formation for rapid bone regeneration.

2. Materials and methods

2.1. Preparation of gelatin methacrylate (GelMA)

GelMA was synthesized based on our previous study [29,31]. Briefly, 20 g gelatin (Sigma-Aldr ich) was dissolved in 200 mL deionized water at 50 °C and then reacted with methacrylic anhydride (MA) (Sigma-Aldrich) for 4 h with continuous stirring at 50 °C. Then, the GelMA solution was dialyzed against deionized water for 7 days at 40 °C. After 7 days, the GelMA solution was frozen overnight at −80 °C and then lyophilized. After lyophilization, the GelMA foam was stored at −20 °C for further use. Finally, 1H nuclear magnetic resonance (NMR, AVANCE III) was performed to characterize the double bond formation, verifying the successful synthesis of GelMA.

2.2. The synthesis of the photo initiator (LAP)

Lithium phenyl-2,4,6-trimethylbenzoylphosphinate (LAP) was synthesized according to a published research [32]. Briefly, dimethyl phenylphosphonite (Ourchem) was reacted with 2,4,6-trimethylbenzoyl chloride (Sigma–Aldrich) via a Michaelis-Arbuzov reaction. Then, 2,4,6-trimethylbenzoyl chloride was added to dimethyl phenylphosphonite in a continuously stirred state at room temperature, protected by argon gas. The mixed solution was stirred for 18 h whereupon lithium bromide (Aladdin) in 2-butanone (Sinopharm Chemical Reagent) was added to the mixture and then the reaction mixture was heated to 50 °C for the formation of the solid precipitate. The solid precipitate was collected and washed by 2-butanone.

2.3. hBMSC and rabbit-derived BMSCs isolation and culture

Human bone marrow-derived stem cells (hBMSCs) were obtained from femur of patients undergoing fracture operation with approval of Research Ethics Committee of the First Affiliated Hospital, College of Medicine, Zhejiang University (ZJU2018392). hBMSCs were isolated by filtrating bone marrow through a 40 μm cell strainer (Corning Inc, Corning, NY, USA). After filtering, the cells were centrifuged, resuspended and cultured in 95-mm dishes in L-DMEM complete growth

medium. The cells were then cultured in incubator with 5% CO_2 at 37 °C for 3–4 days. Then, the adherent cells were passaged into new flasks. For rabbit-derived BMSCs isolation, male rabbits (3 weeks old) were sacrificed by cervical dislocation and rinsed in 75% ethanol. Then, the femurs were removed intactly and stored on ice in L-DMEM supplemented with 1% P/S while waiting for further dissection. After removing the muscle and connective tissue, sterile surgical instruments were used to cut the ends of the femurs. A needle attached to a syringe containing basal L-DMEM medium was inserted into the spongy bone to flush the bone marrow out of the cut end of the femur. The bone marrow was collected in a 10-mL tube. The following steps were the same as the protocol for hBMSCs isolation.

2.4. Fabrication of hBMSC/rBMSC-containing GelMA MSs

MSs were fabricated with a custom-made DLP 3D printer. The size of MSs was digitally defined by Computer Aided Design (CAD) software. More than 7000 MSs can be printed once within minutes. The light wavelength of the DLP machine is 385 nm and the energy density ranges from 0 to 150 mV/cm^2. The model of MS specimens was generated by CAD software and exported as STL file. Then, the STL file was sliced for 3D printing. The parameters including exposure time, 2000 ms, light intensity, 75 mV/cm^2, and the thickness of each slice layer, 20 μm, were used for further printing. 10% (w/v) GelMA solution was chosen to fabricate cell-containing MSs based on our previous work [29]. The final bioink formula consists of 10% GelMA, 0.1% LAP and 0.04% phenol red (Sigma-Aldrich Co, Ltd, USA), which acts as the UV absorber. The bioink was filtered with 0.22 μm filter to get sterile bioink solution. The printing process was divided into the following two steps (Fig. 1A): 1) preparation of bioinks with high density of hBMSCs; 2) printing of cell-loaded MSs by 3D printer. Firstly, for the fabrication of 3D printed GelMA MSs containing hBMSCs (for *in vitro* experiments) and rabbit-derived BMSCs (rBMSCs) (for *in vivo* experiments), cells were mixed homogenously in the bioink with the concentration of 2×10^6 cells/mL to achieve cell aggregation and condensation within the MSs. Then, the cell-laden bioink was added in the ink reservoir after DLP machine was sterilized by ultraviolet irradiation. GelMA MSs containing hBMSCs/rBMSCs were printed automatically. After printing was done, the printed MSs were removed from the printing platform to the petri dish with growth medium for further *in vitro* culture. More than 7000 MSs can be fabricated by printing once. MSs were cultured in growth medium or induction medium for further experiments.

2.5. Cell viability and morphology within MSs

Live/Dead staining was utilized for cell viability measurement. After 7, 14, 21, 28 and 35 days of culture, the cell-loaded MSs were washed by PBS, and fresh medium containing 0.2% (v/v) Calcein-AM (DOJINDO Chemical Technology Co, Ltd, Japan) and 0.02% (v/v) Propidium Iodide (DOJINDO Chemical Technology Co, Ltd, Japan) was added for Live/Dead staining. After 30 min of incubation at 37 °C, the samples were washed by fresh medium and visualized with the confocal laser scanning microscope (BX-FV1000, Olympus, Tokyo, Japan). Two images of each frame were required: green for live cells and red for dead cells. Cell number and cell viability were analyzed by Imaris software and calculated by Microsoft Excel. For each sample, six biological replicates were prepared and three technical replicates were repeated.

The morphology of cells within MSs was observed by staining of Rhodamine Phalloidin (Cytoskeleton, Hangzhou qiongsheng Technology Co, Ltd, China) and DAPI (Beyotime Co, Ltd, China). Briefly, after 7, 14, 21, 28 and 35 days of culture, MSs were washed by PBS first and then fixed by using 4% (w/v) paraformaldehyde (30 min at room temperature). After fixation, the samples were washed by PBS for 3 times, 5 min for each time. Then, the samples were treated by PBS containing 1% (v/

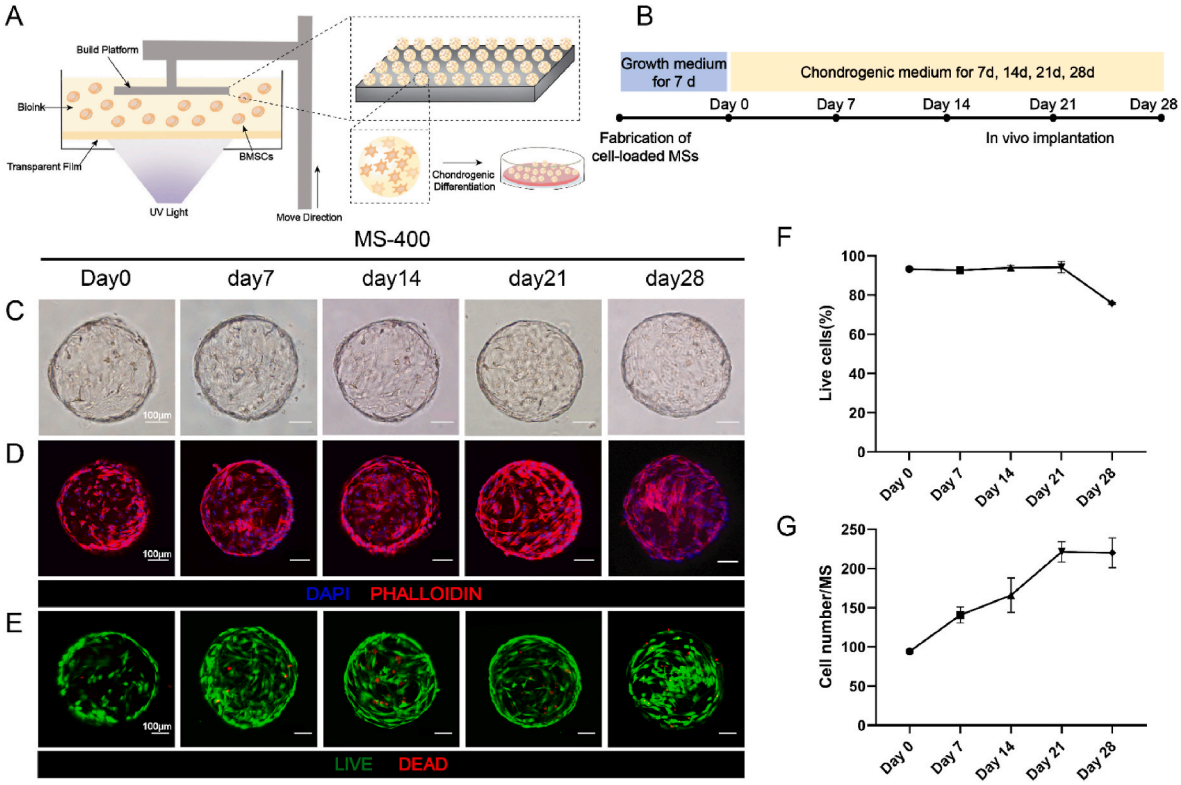

Fig. 1. Fabrication and long-term culture of BMSCs-loaded MSs. A) Illustration of BMSC-loaded MSs fabrication by 3D printing; B) Timeline of *in vitro* culture (complete growth medium for 7 days and chondrogenic differentiation medium for 28 days); C) Representative bright field images; D) Confocal z-projection images of phalloidin/DAPI staining and E) live/dead staining of BMSCs cultured in MSs without induction (day 0), at day 7, day 14, day 21 and day 28; F) Cell viability (%) of MSs over time; G) Cell number per MS over time. (scale bar = 100 μm in C-E).

v) phalloidin for 30 min and then washed by PBS. The MSs were then immersed in PBS containing 0.1% DAPI for 10 min and then washed by PBS. After staining, the samples were visualized with the confocal laser scanning microscope and analyzed by Imaris software. All the Live/Dead images and phalloidin images were acquired by Z-stack function to get single images.

2.6. Chondrogenic differentiation of MSs

For chondrogenic induction, 500 μL of MSs were cultured in low adhesion 6-well plate each well with 4 mL of chondrogenic medium. The chondrogenic medium was composed of H-DMEM supplemented with 1% P/S, 1% sodium pyruvate (Thermo Fisher Scientific-Gibco Co, Ltd, USA), 1% insulin transferrin selenium (Thermo Fisher Scientific-Gibco Co, Ltd, USA), 1×10^{-7} dexamethasone (Sigma-Aldrich Co, Ltd, USA), 50 μg/mL ascorbic acid (Sigma-Aldrich Co, Ltd, USA) and 10 ng/mL TGF-β_3 (Novoprotein Co, Ltd, China). The chondrogenic medium was replaced half every 2 days.

2.7. Fabrication and chondrogenic differentiation of hBMSC pellets

3×10^5 hBMSCs were added to each 15 mL centrifuge tube, and were immersed in 1 mL chondrogenic medium for the fabrication of pellets. Other procedures of chondrogenic differentiation of pellets were the same as MSs.

2.8. Quantitative real-time PCR analysis

TRIzol (Takara) was utilized to extract the total RNA and then the RNA was reverse-transcribed cDNA through the use of HiScript II Reverse Transcriptase (Vazyme). qRT-PCR was further performed on a Light Cycler apparatus (Roche 480II) using SYBR Green qPCR Master Mix (Takara). The primers of Sox 9, Col2a1, Col10a, IHH, Runx 2, Osterix and VEGF are listed in Table S1 and GAPDH was used for the normalization of data. The relative differences in expression of target genes were calculated using the $2^{-\triangle\triangle Ct}$ method.

2.9. Immunofluorescence, alcian blue and alizarin red staining of in vitro MSs and pellets

MSs were washed and fixed by following the steps in cell morphology analysis mentioned before. After fixation, the samples were washed by PBS three times and blocked in 5% bovine serum albumin for 1 h at room temperature. Then the samples were incubated with primary antibodies at 4 °C overnight. After washed by PBS, the samples were incubated with fluorescein-conjugated secondary antibodies for 1.5 h and cell nuclei were stained by DAPI (Beyotime) for 10 min. Stained samples were observed under a confocal microscope system (BX-FV1000, Olympus, Tokyo) and analyzed by Imaris software. All the immunofluorescent images were acquired by Z-stack function to get single images. The primary antibodies were listed as follows: SOX9 (Abcam, ab185966), COL2 (Abcam, ab34712), RUNX2 (Abcam, ab76956), OSX (Abcam, ab22552). For Alcian Blue and Alizarin Red staining, after washing and fixation, the MSs were stained by Alcian Blue overnight and Alizarin Red for 30 min. The MSs were washed by PBS until the PBS was no longer distorted. The MSs were observed under microscope (Olympus, Tokyo).

2.10. Bulk RNA sequencing and data analysis

The gene expression of several groups including untreated BMSCs (control), MSs without induction (MS 0 d), MSs after chondrogenic induction for 7 days (MS 7 d), 21 days (MS 21 d), and pellets after chondrogenic induction for 7 days (pellet 7 d) and 21 days (pellet 21 d) as control groups was investigated by RNA sequencing (Fig. 3A). RNA-seq reads data were mapped to (human, hg38. p5) reference genome using Spliced Transcripts Alignment to a Reference (STAR) software [33]. Expression was calculated with counts per million (CPM). Bioconductor's edgeR R package (v 3.30.3, Robinson and Oshlack, 2010) was used to calculate differentially expressed genes. Gene Ontology and KEGG enrichment were generated with Bioconductor's cluster Profiler R package (v 3.16.1) and their distribution was plotted using ggplot 2 R package (v 3.3.2). All heatmaps were created using the heatmap R package (v 1.0.12) from a list of manually selected genes.

2.11. Single-cell RNA sequencing and data analysis

Cells from the clinical phalange tissues in early childhood (4 samples from 9 months to 8 years old) were isolated. The procedure was approved by Children's Hospital of Zhejiang University School of Medicine ethics committee (No. 2020-IRB-077). The bone and cartilage tissues were isolated and digested in 2% collagenases for 4 h. The single cell suspension was collected, and mRNA libraries were prepared by 10 × Genomics and sequenced on an Illumina HiSeq X™ (Illumina, Cat# FC-502-2021). For quality control, the counts data were normalized with CPM (counts per million), and all the cells with feature number lower than 1000 or higher than 7000 were removed. Cells with transcripts from mitochondrial genome occupying more than 50% in their library were removed. After filtering, the Seurat object was generated from digital gene expression matrices. Fourteen principal components were used in cell cluster with the resolution parameter set at 0.4. Cell cluster was performed and UMAP marker genes were outputted to define each cell cluster.

2.12. Similarity score analysis

N = 4 for CPM of Bulk sample and reference single-cell dataset were normalized and log-transformed following Single R pipeline. Similarity score was calculated with wilcox DE method and default parameters by Single R function in R package.

2.13. In vivo degradation of GelMA MSs

300 μL volume of pure GelMA MS deposits (about 9000 MSs) after centrifugation (1200 rpm for 5 min, immersed in basal DMEM) were subcutaneously injected in rats (male, 25-week-old) by 1 mL syringe with 23-gauge needle. After 1, 2 and 4 weeks of implantation, the samples were taken out for weighing (n = 3) and frozen section (n = 3). For weighing, the MSs were taken out from subcutaneous tissues and weighed in Ep tube. For frozen section, the samples were fixed in 4% (w/v) paraformaldehyde and the sample slides at 10 μm were obtained by a frozen section process. H&E staining was performed to investigate the degradation of MSs.

2.14. In vivo implantation of MS constructs

For subcutaneous injection, MSs were immersed in basal DMEM and centrifugated (1200 rpm for 5 min) to get the MS deposits. 100 μL volume of MS deposits (about 3000 MSs) of each group was injected subcutaneously by 1 mL syringe with 23-gauge needle. Pure MSs, BMSCs-loaded MSs (with the same treatment with osteo-callus group but without induction) and osteo-callus organoids were injected subcutaneously in immunodeficient mice (BALB/c Nude, male, 8-week-old), 3 mice for each group. Subcutaneous implants were taken out after 4 weeks. The samples were fixed in 4% (w/v) paraformaldehyde overnight for subsequent histological and immunofluorescent analysis.

For in-situ repair of bone defects in rabbits, twenty-four male New Zealand rabbits (3-month-old, 2.5–3 kg) were chosen. The rabbits were randomized into four groups: Blank defects, pure MSs, BMSC-loaded MSs and osteo-callus organoids (n = 6 rabbits per group). A 5 mm in diameter and 4 mm in depth defect was created by using electric drill in distal femur. Briefly, the rabbits were anaesthetized with Pentobarbital (3% (w/v), 1 mL/kg, Merck) and a 20 mm longitudinal incision was

made along the distal femur. After the skin and muscle were separated, defects with size mentioned above were made and 100 μL volume of MS deposits (about 3000 MSs) were implanted with MSs (blank defect without implantation). The incision was closed and the rabbits were given intramuscular injection of penicillin 10 000 units per day for three consecutive days. All protocols were approved by the Zhejiang University Ethics Committee (ZJU20210239). The rabbits were sacrificed with an overdose of Pentobarbital for subsequent Micro-CT, histological and immunohistochemical analysis.

2.15. Quantification of micro-CT

After 4 weeks of animal surgery, the femur samples were fixed in 4% paraformaldehyde for 3 days. Micro-CT equipment (U-CT-XUHR, Milabs) was applied for 3D scanning of the samples. A cylindrical region (5 mm in diameter, 4 mm in depth) was defined to analyze the bone regeneration within the defect site. After 3D reconstruction, images of whole distal femur and defect site were obtained. The bone tissue volume/total tissue volume (BV/TV), bone mineral density (BMD), trabecular thickness (Tb. Th) and trabecular separation (Tb. Sp) were automatically determined.

2.16. Histology, immunofluorescence and immunochemistry of subcutaneous and in-situ samples

For histological, immunofluorescent and immunochemical analysis, both subcutaneous and in-situ implantation, the samples were fixed with 4% paraformaldehyde (overnight for subcutaneous samples and 3 days for in-situ samples) after 4 weeks of surgery. Additionally, femur samples were decalcified in Ethylenediaminetetraacetic acid (EDTA) for 6 weeks. Then, the samples were washed by constant flow of water overnight. Then, the samples were dehydrated by a graded ethanol (50%–100%) and cleared in xylene and embedded in paraffin. Ectopic samples were sectioned at 7 μm (subcutaneous samples) and 10 μm (in-situ samples) with a slicer (Leica). Histology including H&E, Masson's Trichrome and Safranin O staining was performed according to previously reported research. For immunofluorescent staining, all sections were blocked in 5% bovine serum albumin for 1 h after dewaxing and permeabilization before incubated with primary antibodies at 4 °C overnight. The primary antibodies used in subcutaneous samples were as follows: COL2 (Abcam, ab34712), OCN (R&D, MAB1419), CD31 (Abcam, ab182981). The primary antibodies used in rabbit samples were as follows: CD31 (Novus, NB600-562), OCN (Novus, NB100-6280), COL1 (Novus, NB600-408), COL2 (Novus, 600–844). Following washing with PBS, the samples were incubated with fluorescein-conjugated secondary antibodies for 1.5 h and cell nuclei were visualized by DAPI (Beyotime). Stained histology sections were observed under a confocal microscope system (BX-FV1000, Olympus, Tokyo, Japan). For immunohistochemistry analysis, after incubated with primary antibodies at 4 °C overnight and washed by PBS, sections were incubated with horseradish peroxidase (HRP)-linked secondary antibodies (Jackson, 111-035-003) for 1.5 h and then visualized with 3, 3-diaminobenzidine solution (DAB, ZSGB-BIO).

2.17. Transmission electron microscope (TEM) analysis of femur samples

For TEM analysis, harvested femur samples were fixed by glutaraldehyde and observed by TEM (100 kV technical 10, center of cryo-electron microscopy, Zhejiang University).

3. Results

3.1. DLP-based 3D bioprinting successfully fabricate the BMSCs-loaded MSs

Mesenchymal condensation is the initial process of osteo-callus formation in endochondral ossification [6]. In this study, stem cell condensation *in vitro* was realized by the fabrication of BMSCs-loaded GelMA MSs by a custom-made digital DLP-based 3D printer [34]. The number of cells per MS was adjusted by the initial cell density of inks (2×10^6 cells/ml). According to the diameters set by CAD software, GelMA MSs loaded with BMSCs with diameters of 200 μm (MS-200), 400 μm (MS-400), and 600 μm (MS-600) were successfully fabricated (Fig. S1A). Then, MSs with different diameters were cultured *in vitro* for 5 weeks in complete growth medium. The cell number and cell viability of MSs with different sizes were analyzed. Live/Dead assay and its quantitative analysis showed that MSs with a larger diameter (MS-600) were capable of loading more cells but negative for cell viability, which was probably due to limited oxygen and nutrition transportation (Figs. S1B–E). Cell viability of MS-200 was similar to that of MS-400 (Figs. S1B–E). Interestingly, the number of cells per volume in MSs with different diameters indicated MS-400 had the optimum ability to carry cells (Fig. S1F). Considering the balance between the cell loading ability and the cell viability, we therefore chose MS-400 in this study for further analysis.

To mimic the initial differentiation process of endochondral ossification, the BMSCs-loaded MSs were induced in chondrogenic medium for 4 weeks closely after 1 week of expansion in complete growth medium (Fig. 1B). As shown in Fig. 1C and D, bright-field images and Filamentous-actin (F-actin) staining demonstrated the typical polarized spindle morphology of BMSCs cultured in the printed MSs. Live/Dead staining revealed that the majority of cells in the MSs were viable till 4 weeks after chondrogenic induction; however, there was also a mild increase in dead cells after the total 5 weeks of long-term culture *in vitro* (Fig. 1E and F). Moreover, the cell number in each MS increased during 4 weeks and became stable after 5 weeks (Fig. 1G), indicating a decrease in proliferation rate. Such decrease in cell proliferation was also observed in endochondral ossification process, which indicated cellular maturation in MSs [35].

The above results indicated fabrication of cell-loaded MSs was successfully realized through DLP-based 3D bioprinting. Moreover, during chondrogenic differentiation, the BMSCs-loaded MSs showed high cell viability and survived up to 5 weeks *in vitro*, showing the feasibility of mimicking osteo-callus formation.

3.2. Chondrogenic MSs undergo endochondral ossification processes in vitro

During endochondral ossification or bone healing process, the mesenchymal condensations will differentiate into soft callus which would ultimately become hypertrophic and calcified. Considering the balance between the cell viability and *in vivo* implantation, MSs cultured for 4 weeks (7 days in complete growth medium and 21 days in chondrogenic differentiation medium) were analyzed in further research. To analyze the differentiation stages of the MSs, immunostaining and qPCR of relevant biomarkers during the stage of callus formation in endochondral ossification [13] were performed. Pellets, as a conventional culture model for cell aggregation and chondrogenic differentiation, were also analyzed after induction as a comparison. The early chondrogenic transcription factor sex-determining region Y box 9 (SOX9) was strongly expressed in both MSs (Fig. 2A, **2B)** and pellets (Figs. S2A and 2B) during 21 days' chondrogenic induction. Notably, the expression of SOX9 in MSs was slightly decreased in the late stage of differentiation (day 14 and 21) (Fig. 2A, B, 2D), while it continuously increased during the whole chondrogenic induction in pellets group (Figs. S2A and S2B), indicating the transformation of early chondrogenic state into mature chondrogenic situation in MSs. To further define the chondrogenic efficiency of MSs, the expression of chondrocyte phenotype marker, type 2 collagen (COL2), was analyzed. Together with the qPCR and immunostaining results (Fig. 2D), the expression of COL2 was gradually increased after 7 days' (positive cells, ~35.65%) chondrogenic differentiation within MSs and strongly expressed at day 14 (positive cells, ~78.38%) and day 21 (positive cells, ~90.01%) (Fig. 2A

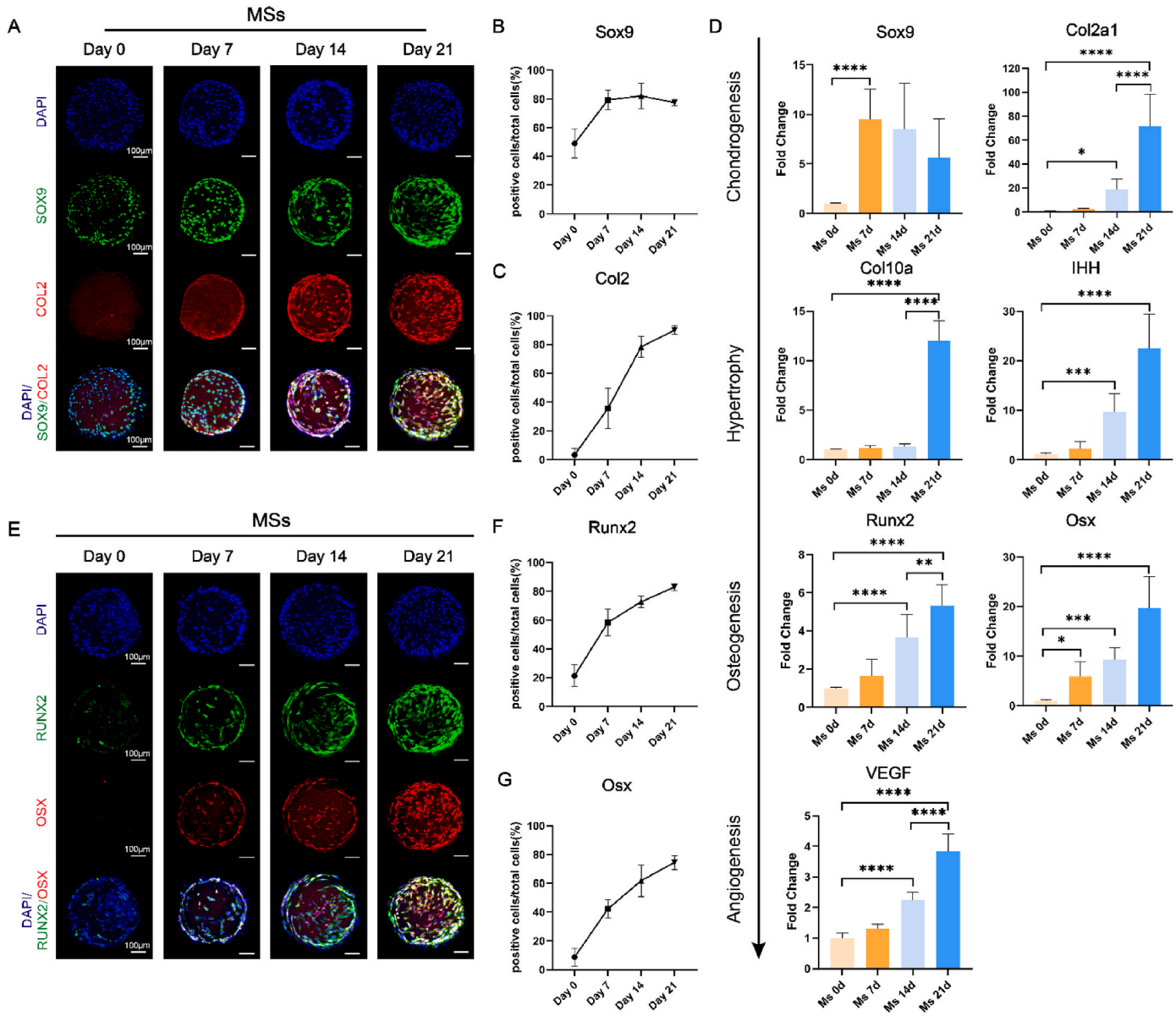

Fig. 2. MSs undergo endochondral ossification processes under chondrogenic differentiation. A) Representative confocal z-projection images of SOX9 and COL2 immunofluorescent staining of BMSCs in MSs without induction (day 0), at day 7, day 14 and day 21 of chondrogenic induction; B–C) The percentage of SOX9 (B) and COL2 (C) positive cells in MSs over time; D) Quantification of mRNA transcript of chondrogenic, pre-hypertrophic/hypertrophic, osteogenic and angiogenic gene markers, normalized to non-induction (n = 3 mean value ± SEM), *p < 0.05, **p < 0.01, ***p < 0.001, ****p < 0.0001, one-way ANOVA followed by Tukey's multiple comparison test; E) Representative confocal z-projection images of RUNX2 and OSX immunofluorescent staining of BMSCs in MSs without chondrogenic induction (day 0), at day 7, day 14 and day 21 of chondrogenic differentiation and F-G) quantitative analysis of positive cells (%) (F, RUNX2; G, OSX). (scale bar = 100 μm in A, E).

and C). Alcian Blue staining of MSs was also presented as a proof of chondrogenic state after induction (Fig. S2G). On the contrary, the expression of COL2 in pellets was not observed until 14 days (~42.95%) of chondrogenic induction, and apparently increased at day 21 (~73.92%) (Fig. S2A, 2C), demonstrating a delayed collagen synthesis in pellets compared with MSs.

As shown in Fig. 2D, gene expressions of hypertrophic markers collagen type X alpha 1 chain (COL10A1) and In·dia hedgehog signaling molecule (IHH) were significantly upregulated at day 14 and 21 in the MSs. The expression of Runt-related transcription factor 2 (RUNX2), which was expressed in pre-hypertrophic chondrocytes and osteoblasts, was slightly upregulated after 7 days of chondrogenic differentiation and continued to increase after 14 days and 21 days (Fig. 2E and F) in the MSs. As a marker for osteogenesis, osterix (OSX), directly regulated by RUNX2, was also remarkably expressed in the latter stage of chondrogenic differentiation in the MSs (Fig. 2E and G). The qPCR analysis of RUNX2, OSX and Alizarin Red staining double confirmed the corresponding hypertrophic and osteogenic state presented in the MSs (Fig. 2D, Fig. S2H). On the other hand, pellets showed similar tendency toward the expression of RUNX2 and OSX over time but with a relatively lower level and delayed expression (Figs. S2D–F). In addition, the transformation from cartilage to bone in endochondral ossification is proceeded by the invasion of blood vessels in hypertrophic cartilage core. The expression of Vascular Endothelial Growth Factor (VEGF) was significantly upregulated after 14 and 21 days in the MSs (Fig. 2D), showing the similarity between the MSs and native callus development. In another word, the chondrogenic MSs simulated osteo-callus formation in endochondral ossification which prompt BMSCs to undergo

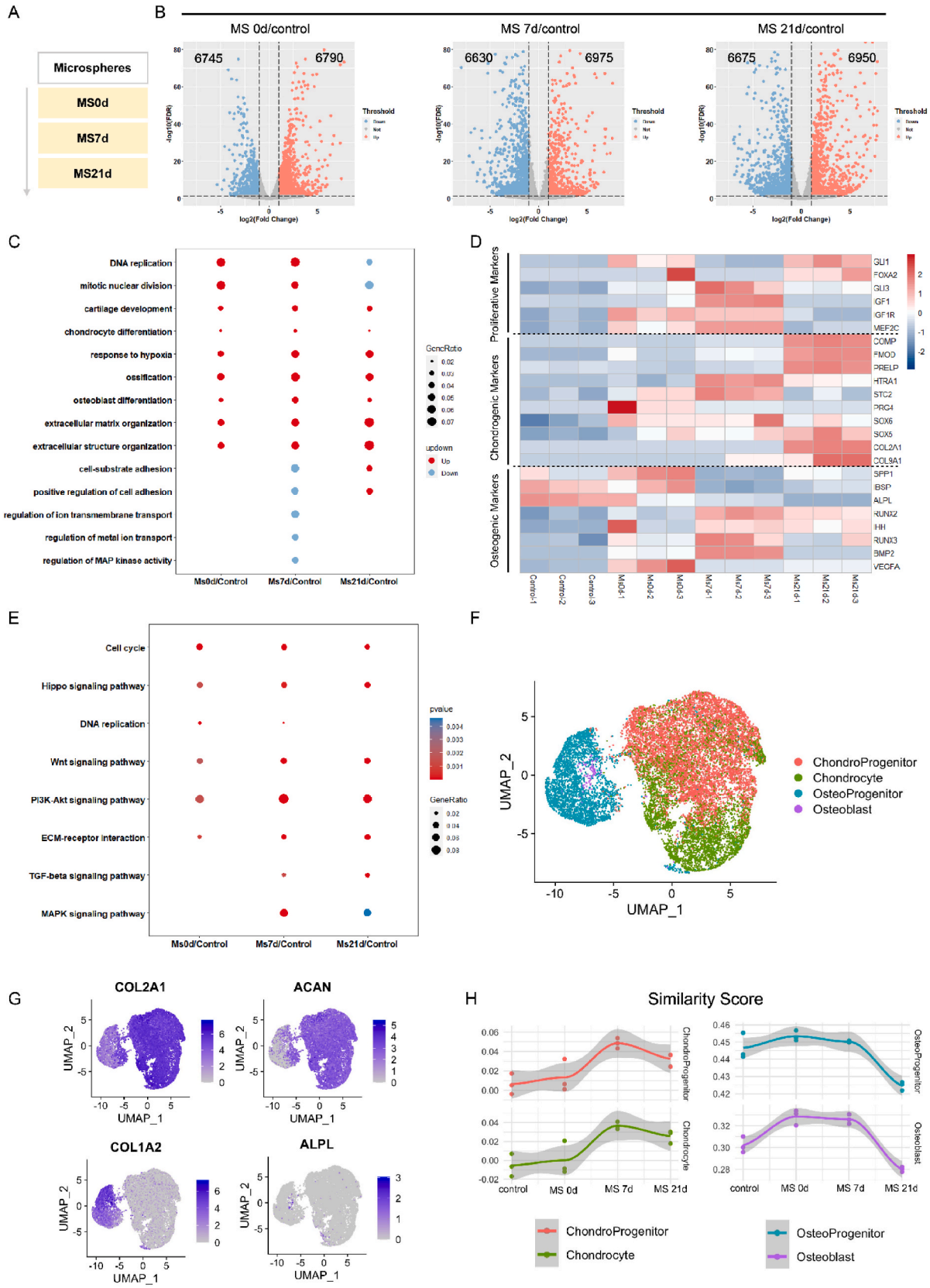

Fig. 3. RNA-seq analysis of BMSCs in MS culture system over time. A) Schematic illustration of groups for RNA-seq; B) Clustering for differentially expressed genes ($p < 0.05$ and $\log_2$-fold > 1) in control and MS group over time (MS 0 d, MS 7 d, MS 21 d); C) Analysis of enriched biological processes in MS group compared with control; D) The heatmap of differentially expressed genes regulating endochondral ossification about stem cell proliferation, chondrogenic and osteogenic differentiation in MSs over time; E) Signaling pathway analysis by KEGG of differential genes associated with proliferation and differentiation; F) Visualization of cell heterogeneity in reduced dimensions of Uniform Manifold Approximation and Projection (UMAP); G) Expression of cell type specific markers in UMAP visualization; H) Similarity score of samples at different time with the single-cell reference of 4 cell types; The similarity score was calculated by Single R [39].

proliferation, chondrogenic differentiation, subsequent hypertrophic as well as osteogenic maturation and blood vessel invasion.

3.3. MSs follow endochondral ossification gene expression patterns and transform into osteo-callus organoids during chondrogenic differentiation

To deeply gain insight into the cell differentiation in MSs system, bulk-RNA sequencing and data analysis were performed. The upregulated genes (MS 0 d, 6790 genes; MS 7 d, 6975 genes; MS 21 d, 6950 genes) and down regulated genes (MS 0 d, 6745 genes; MS 7 d, 6630 genes; MS 21 d, 6675 genes) over time among all detected genes with significantly regulated expression ($p < 0.05$ and $\log_2$-fold > 1) in chondrogenic MSs group compared with control (the newly fabricated MSs) were shown in Fig. 3B. To further understand the signaling actions during the chondrogenic differentiation in MSs culture system, the biological processes enriched by these differentially expressed genes (DEGs) were investigated by Gene Ontology (GO) analysis (Fig. 3C). Results showed that the upregulated DEGs in MSs culture were enriched for chondrogenic differentiation, osteogenic differentiation and extracellular organization, and were continuously upregulated during the whole chondrogenic induction. Interestingly, it was found that in the early stage of the chondrogenic induction (MS 0 d and MS 7 d), cell division-related GO terms, such as "DNA replication" and "mitotic nuclear division", were significantly upregulated, suggesting that stem cells within the MSs culture system showed a simultaneous cell proliferation and differentiation state. More specifically, as shown in Fig. 3D, featured biomarkers related to stem cell proliferation (such as GLI1, FOXA2, GLI3, IGF1) were mainly upregulated during the first phases (MS 0 d and MS 7 d). From day 7 onward, the biomarkers that related to chondrogenic differentiation (such as COMP, PRG4, SOX6, SOX5, COL2A1, COL9A1) and osteogenic differentiation (SPP1, IBSP, ALPL, RUNX2, IHH, RUNX3, BMP2) were basically upregulated when compared with control. The stage-dependent gene expression indicated that this was mirrored in the gene expression pattern that was involved in endochondral ossification process. In addition, the KEGG pathway analysis further revealed that significantly regulated genes were enriched in cell proliferation-related signaling pathways (Cell cycle, Hippo signaling pathway and DNA replication) and stem cell differentiation-related signal pathways (Wnt signal pathway, PI3K-Akt signaling pathway, ECM-receptor interaction, TGF beta signaling pathway and MAPK signaling pathway), which conformed with gene expression pattern in bone development (Fig. 3E). The above results showed the potential of MSs culture system in maintaining both stem cell self-renewal and differentiation at transcriptional level, as well as the advantages in biomimicking the complicated cell fate and enlargement of cartilage core *in vivo*.

To further explore the advantages of MSs culture system over the traditional pellet model, well-known genes for cell proliferation and differentiation were analyzed. The expression of genes related to stem cell proliferation and osteogenic differentiation were upregulated to a much higher level in MSs when compared with pellet (Fig. S3A). The coexistence of cell proliferation and differentiation supported by MSs culture system is more similar to the stem cell maintenance and rapid morphogenesis that underly the skeletal bone tissue development, while subsequent GO enrichment analysis also conformed this scenario (Fig. S3B). Notably, the expression of CXCLs (including CXC1L, CXCL2, CXCL3, CXCL5, CXCL6, CXCL8) was widely upregulated at all time points of chondrogenic induction in MSs groups. GO enrichment analysis of these differentially expressed genes showed the upregulation of cytokine production (regulation of response to cytokine stimulus, positive regulation of cytokine production and cytokine secretion) in the MSs group (Fig. S3B). It has been proven that CXCLs especially CXCL6, mediated by AKT signaling, were expressed in healthy cartilage and played a crucial role in maintaining homeostasis for articular cartilage [36]. KEGG pathway analysis in our data also revealed the activation of PI3K-AKT signaling pathway in the MSs culture system, which provides a possible mechanism for its advanced stem cell proliferation and differentiation potential (Fig. 3D). Therefore, the alterations in CXCL secretion could partly help explain the upregulated stem cell viability partly through PI3K-AKT signaling pathway, however, the further mechanism is still to be explored.

Interestingly, through the comparison of the bulk-RNA data of cultured BMSCs in MSs at varied time points with the single-cell RNA Seq data of the clinical phalange tissue samples in early childhood, we found that the *in vitro* cultured BMSCs within MSs share high similarities both in diverse cell compositions (2 mesenchymal progenitors, chondrocytes and osteoblasts) and cell states (under self-renewal and differentiation) with the 4 cell subpopulations (Fig. 3F and G), as revealed by the similarity score (Fig. 3H). Actually, during native long bone development, undifferentiated mesenchymal cells that proliferate to restore the growth potential [37] co-exist with osteochondral lineage cells that were activated by several key signals to form mature tissues [38]. Altogether, these results indicated that MSs culture system held a superior capability of maintaining a synchronized state of cell proliferation and osteo-chondral lineage differentiation at transcriptional level (Fig. 3F and G), which highly recapitulates the diverse cell compositions and behaviors involved in the callus formation during endochondral ossification. By this way, the MSs finally transformed into osteo-callus organoids after 21 days of chondrogenic induction.

3.4. Osteo-callus organoids mature and form bone-like tissue in vivo

According to the results of immunofluorescent staining and gene expression, MSs after 21 days of chondrogenic induction were defined as "osteo-callus organoids" in this study. To investigate their capability as building blocks to form large and mature bone-like tissues *in vivo*, 100 μL volume of osteo-callus organoids (Osteo-callus organoids group, about 3000 organoid units), immersed in basal DMEM and obtained by centrifugation (1200 rpm for 5 min) to get the dense organoid deposits, were injected subcutaneously in immunodeficient mice (Fig. 4A). Pure MSs produced by 3D printing but no cell-loaded and BMSC-loaded MSs, with the same treatment with osteo-callus organoids group but without induction, were selected as controls. The equal volume of pure MSs (MSs group) and BMSC-loaded MSs (BMSC-loaded MSs group) immersed in the same buffer after centrifugation were injected for comparison. After 4 weeks of implantation, the constructs containing MSs were analyzed. H&E staining revealed significant blood vessel formation in osteo-callus organoids group compared with other groups (Fig. 4B). Masson's Trichrome staining demonstrated bone-like area around the MSs in osteo-callus organoids group (Fig. 4C), which was not detected in other two groups. Immunofluorescent staining of COL2 and osteocalcin (OCN), a marker of mature bone tissue and a symbol in late stages of mineralization, revealed that chondrocyte activity was prominent in BMSC-loaded MS group, a state of early stage in endochondral ossification, while osteoblast activity was more prominent in osteo-callus organoids group (Fig. 4D), indicating maturation of implanted organoids. The blood vessel formation of the constructs was verified with CD31 immunochemistry staining, and a large amount of CD31 positive cells were detected in BMSC-loaded MSs and osteo-callus organoids group (Fig. 4E, Fig. S5). While no obvious CD31 positive cells can be observed in MSs group (Fig. 4E).

Therefore, BMSCs in MSs without pre-differentiation *in vitro* could be still in the early stage of endochondral ossification after implantation, while the osteo-callus organoids already got mature and attracted blood vessel invasion, further indicating cells in the osteo-callus organoids were in the late stage of endochondral ossification and showed potential to promote bone regeneration *in vivo*.

3.5. Engineered osteo-callus organoids promote rapid healing of bone defects

Based on the results of ectopic implantation, osteo-callus organoids

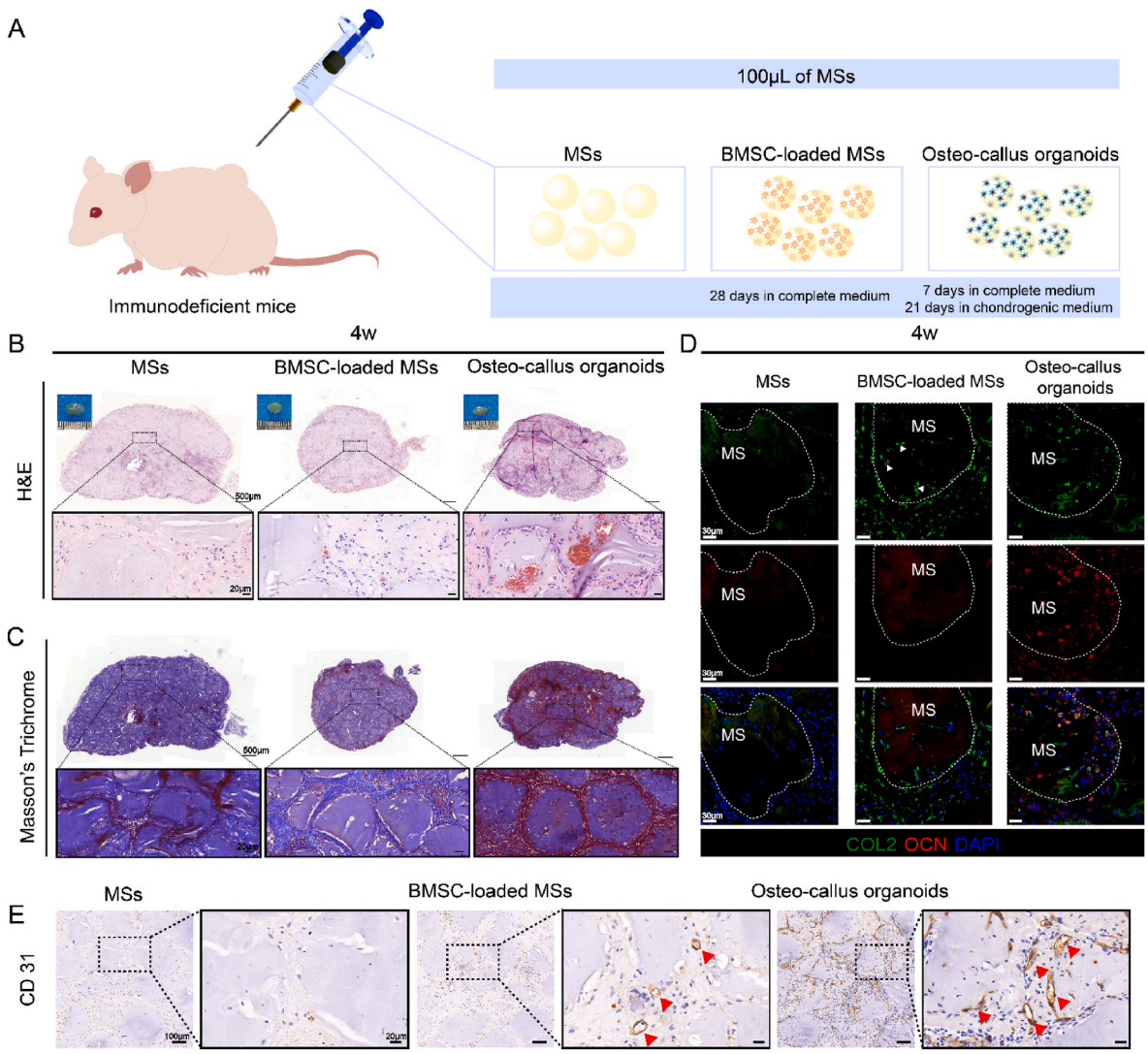

Fig. 4. Assembly of osteo-callus organoids into bone-like tissue. A) Schematic illustration of subcutaneous implantation of different MSs. B–C) Histological evaluations (B, H&E staining; C, Masson's trichrome staining) of MSs after being subcutaneously injected into immunodeficient mice for 4 weeks; Representative images of D) COL2 and OCN co-immunofluorescent staining of implanted MSs and organoids. E) CD31 immunochemistry staining of implanted MSs and osteo-callus organoids. (scale bar = 500 μm in the first row in B and C, 20 μm in the second row in B and C, 30 μm in D, 100 μm in overall figure in E and 20 μm in enlarged figure in E).

were regarded as blocks successfully forming larger bone-like constructs *in vivo*. To explore their capacity to induce in-situ bone regeneration, we implanted osteo-callus organoids into 5 mm × 4 mm cylindrical defects in the distant femur of rabbits (Fig. 5A; Fig. S5A). An empty hole untreated on the femur was regarded as the blank control. Pure MSs and BMSC-loaded MSs were also implanted for comparison to exclude the impact of materials and stem cells (Fig. S5B). After implantation for 4 weeks, rabbits were sacrificed and micro-computed tomograms (micro-CT) analysis was performed to access the new bone formation in different treatment groups. As shown in the reconstructed 3D images, after 4 weeks of implantation, only limited bone tissue was presented around the periphery of defect in blank group and more new bone formation was occurred in MSs and BMSC-loaded MSs group (Fig. 5B). By contrast, much more new bone formation can be observed in osteo-callus organoids group (Fig. 5B). The newly formed bone tissue almost filled the defect sites in osteo-callus organoids group, indicating the almost complete repair of bone defects after 4 weeks of implantation. Quantitative micro-CT analysis further confirmed the significant new bone formation in osteo-callus organoids group (Fig. 5D–F).

Next, histological analysis was applied to provide a more detailed analysis to evaluate the new bone formation efficiency of osteo-callus organoids. H&E and Masson's Trichrome staining confirmed the bone regeneration illustrated by micro-CT. Besides, dense fibrous tissue filled the defect sites and no obvious new bone tissue was formed in blank group. In MSs group, loose fibrous tissue was observed, and collapse of the defect sites indicated the degradation of hydrogel. New bone formation was found at both the periphery and center defects in BMSC-loaded MSs group while abundant new bone tissue was formed at the whole defect sites in osteo-callus organoids group. (Fig. 5G and H). Immunofluorescent staining of CD31 revealed few blood vessel invasions in blank group, indicating dense fibrous tissue formation and no more place for blood vessel ingrowth (Fig. S5A). More CD31 positive cells were observed in MS-containing groups due to the interspace among MSs after implanted in defect sites, which was beneficial for invasion of angiogenic cells (Fig. S5A).

To further confirm the osteochondral fate of osteo-callus organoids after *in vivo* implantation, multiple markers were assessed. As shown in Fig. 6A, significant OCN positive cells were presented in osteo-callus organoids group compared with other three groups, indicating the abundant and mature bone formation. Type I collagen (COL1) is the

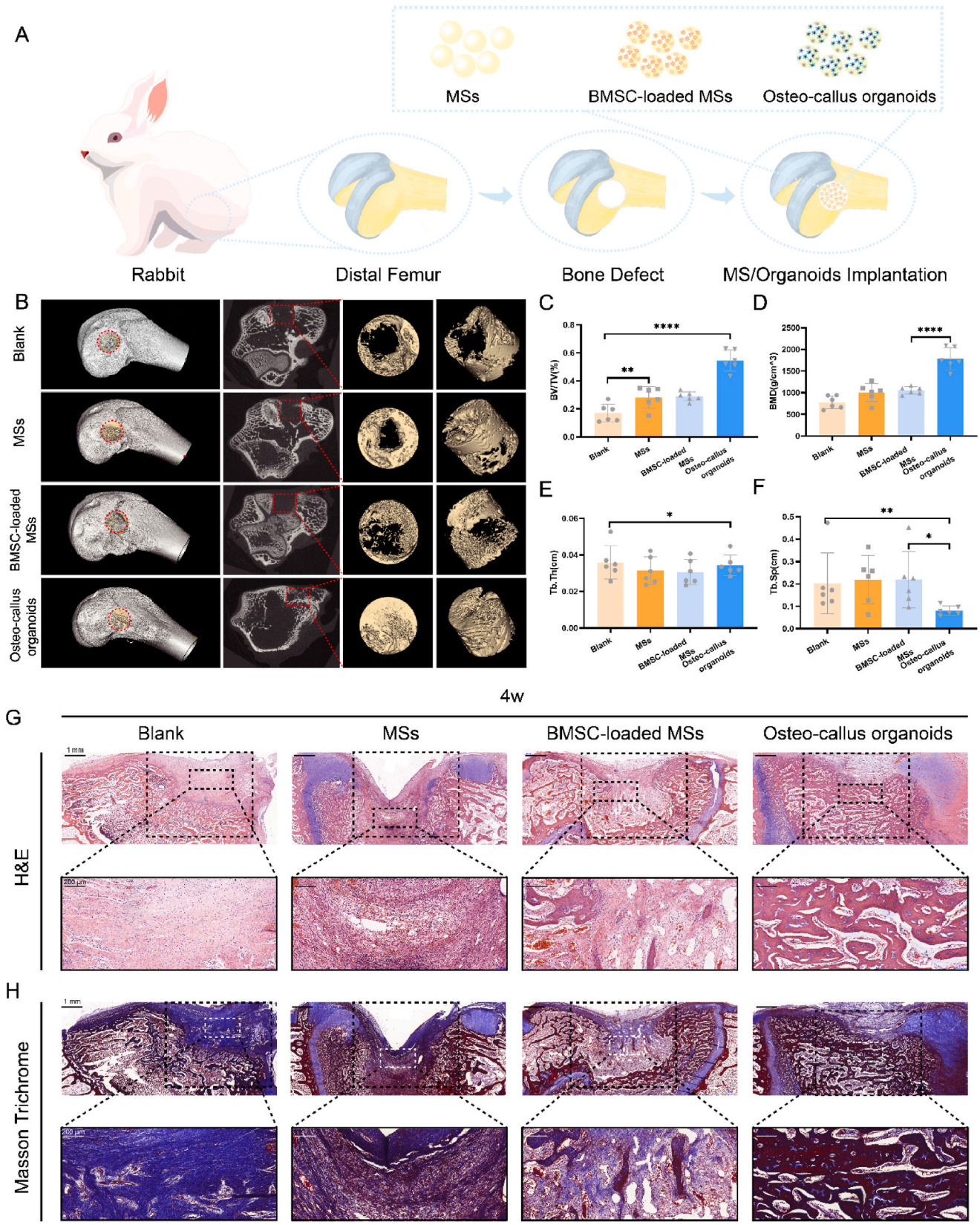

Fig. 5. Micro-CT and histological evaluation of new bone formation after 4 weeks of implantation. A) The schematic illustration of bone defect model of distal femur in rabbits and implantation of pure MSs, BMSC-loaded MSs and osteo-callus organoids; B) Reconstructed micro-CT images of the femur defects (5 mm × 4 mm) in rabbits; C–F) The quantity of the new bone in the defect sites calculated by morphometry analysis: C) BV/TV, the bone tissue volume/total tissue volume; D) BMD, bone mineral density; E) Tb. Th, trabecular thickness; F) Tb. Sp, trabecular separation; Red circles and frames referred to defect sites area; (Data are mean ± standard deviation, n = 6, *$p < 0.05$, **$p < 0.01$, ****$p < 0.0001$); G) H&E and H) Masson's Trichrome staining of femora's section. (scale bar = 1 mm in the first row in G and H, 200 μm in the second row in G and H). (For interpretation of the references to colour in this figure legend, the reader is referred to the Web version of this article.)

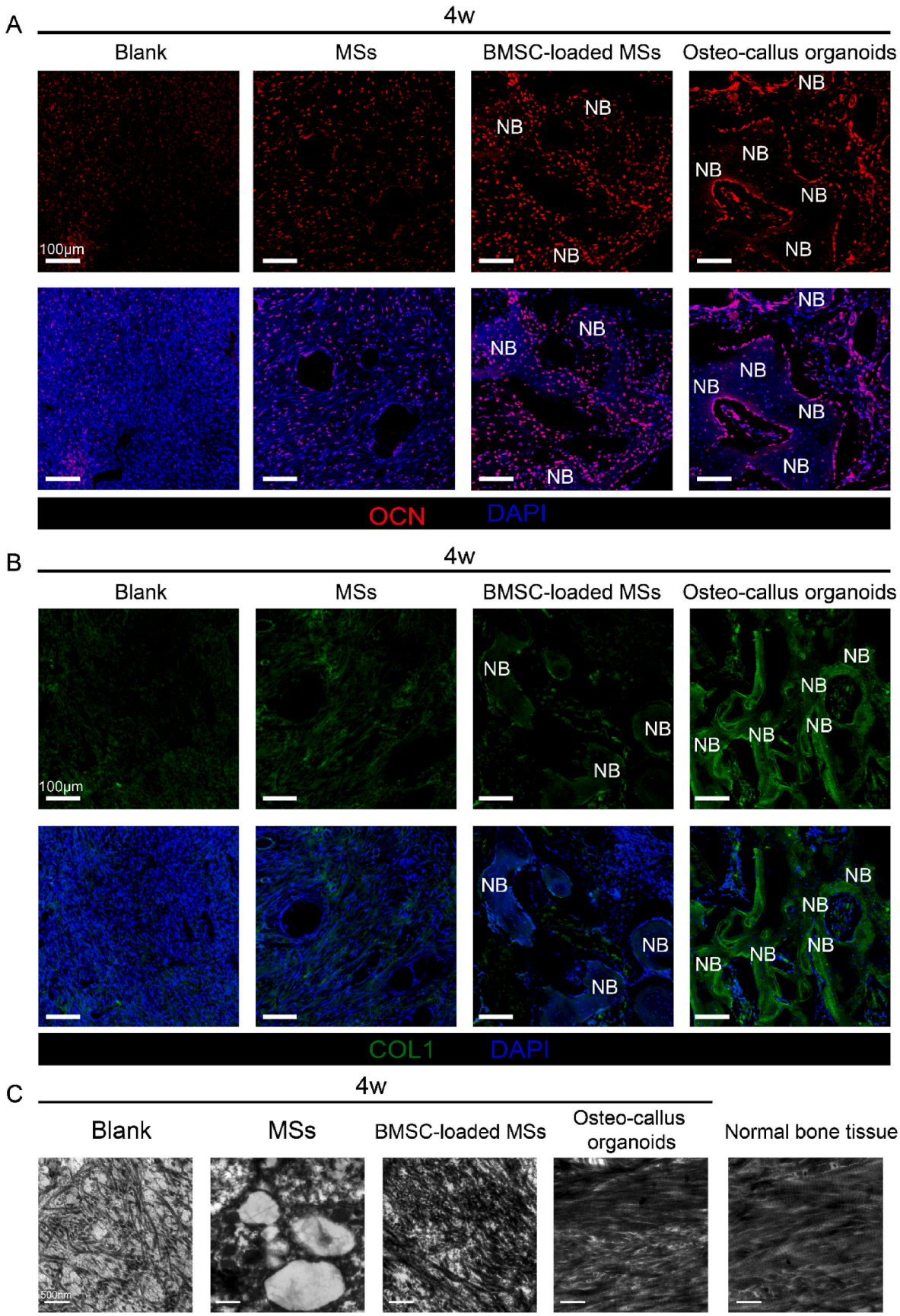

Fig. 6. Immunostaining evaluation of newly formed bone after 4 weeks of implantation. Representative images of sections at the central defect region with immunostaining against A) OCN and B) COL1; C) Collagen appearance of sections in different groups and normal bone tissue shown by TEM. (NB, new bone) (scale bar = 100 μm in A and B, 500 nm in C).

major organic component of the ECM in bone tissue and COL2 is the predominant collagenous component of cartilage. Interestingly, osteo-callus organoids group showed abundant COL1 positive staining with the absence of COL2 staining while BMSC-loaded group was the opposite (Fig. 6B, Fig. S7B). Therefore, the results of immunostaining confirmed that osteo-callus organoids displayed a more mature state than non-induced MSs and pure MSs. Callus tissues and woven bone are dominant tissues in the early stage of fracture healing, and are followed by deposition of lamellar bone in the latter stages of healing. To further identify the structure of newly formed tissue among different groups, transmission electron microscope (TEM) analysis was performed. As shown in Fig. 6C, the new bone tissue in BMSC-loaded MSs group exhibited a disorganized fibril arrangement, while in osteo-callus organoids group, the tissue was characterized by the organized arrangement of collagen fibers into layers or lamellae, which was similar to that in normal mature bone tissue.

Taken together, in-situ implantation of the engineered osteo-callus organoids promoted rapid and mature bone formation within 4 weeks compared to traditional stem cell implantation.

4. Discussion

Developmental engineering-based strategies were proposed for more efficient bone repair. Although developmental strategies have been proven feasible to improve bone formation, the systematically biomimetic processes have not been reproduced. Organoids-based strategies have provided a novel option to solve this problem. However, limitations such as cell source, long-term cell survival and mass production of designed pure cell aggregates-based organoids do exist when applied *in vivo* especially in large defects. In this study, we fabricated hydrogel-based cell aggregates by 3D printing technology to overcome these hurdles. Thousands of cell-loaded MSs can be produced within minutes with a small amount of cell-containing bioink, and cells within the MSs exhibited sustained cell viability during 28 days of *in vitro* culture (Fig. 1; Fig. S1). Moreover, definite control of size and structure of pure cell organoids in current studies is still challenging [40,41]. In this work, the size of printed MSs can be precisely designed by CAD software (Fig. 1; Fig. S1). After *in vitro* chondrogenic differentiation for 21 days, mass production of osteo-callus organoids was realized and provided a new and promising strategy for large bone defect repair.

Interestingly, scaffold-free stem cell aggregates in previous studies based on developmental engineering and scaffold-based organoids in this work both successfully stimulated the gene expression pattern occurred in native endochondral ossification processes, and provided general proof of feasibility in mimicking developmental program *in vitro* at cell level [11,12,42,43]. However, there are some mentionable differences between previous pure cell aggregates and the organoids in this work. When applied subcutaneously, the pure cell aggregates themselves can be easily fused together after implantation due to strong cell-cell interaction and ECM secretion, eventually leading to a thin layer of dense bone formation in the outer surface of the whole implant. In this regard, the scaffold-free approach by cell aggregates may be largely limited for cortical bone defect repair. Consistent with this, a bone marrow cavity was detected in the scaffold-free cell aggregates as early as 4 weeks after subcutaneous implantation [11], indicating a mineralized bone-like organ was formed. While it was indeed beneficial for the repair of cortical bone tissue containing a bone marrow cavity, the newly formed tissue was shown largely from the donor cells themselves. Differently, the implanted osteo-callus organoids in our study exhibited obvious bone formation across the interstitial space of those closely adjacent hydrogel MSs due to the incomplete degradation of materials (Fig. 4B and C; Fig. S4), which provided necessary adhering surfaces and space for the further migration of endothelial cells and endogenous stem cells that are responsible for new bone regeneration. Results from our study also revealed that the implanted osteo-callus organoids were still in a relatively immature hypertrophic state by co-staining of COL2 and OCN (Fig. 4D), indicating an active callus-like phenotype which supports further vascularization and subsequent endogenous ossification. Therefore, when utilized as micro-niches for further bone formation *in vivo*, the hydrogel MSs-based callus-like organoids could be more suitable for the regeneration of large-sized bone defects, especially cancellous bone.

Osteo-callus is a highly heterogeneous tissue and contains different types of cells, in which the cell proliferation, chondrogenic and osteogenic transformation are intensely regulated during endochondral ossification. Together with positive green in Safranin-O staining, the osteogenic marker genes of cell aggregates in previous study were strongly expressed in advance as early as day 7 after chondrogenic induction [11]. In our study, RNA seq analysis of cells within osteo-callus organoids demonstrated an early expression of chondrogenic marker genes and a gradually increased expression of osteogenic markers (Fig. 2D). Obviously, the pure stem cell aggregates were more differentiated and hypertrophic than cells in the hydrogel MSs-assisted cell condensation. In addition, further GO enrichment analysis revealed a unique coexistence of proliferation, chondrogenic and osteogenic differentiation in the MS-based cell culture system. In addition, the bulk-RNA seq data of cells from osteo-callus organoids showed high similarity in cell states (self-renewal and differentiation) and cell compositions (chondro-progenitor cells, osteo-progenitor cells, chondrocytes and osteoblasts) compared with that in the single-cell RNA seq data of clinical phalange tissue in early childhood, which undergoes an active phase of endochondral ossification. To the best of our knowledge, such high similarity at transcriptomic profile between engineered osteo-callus organoids and developmental bone tissues in cell states and compositions has not been reported elsewhere so far. Compared with conventional cell aggregates, the MSs culture system provides a more efficient and biomimetic platform to construct callus-like organoids *in vitro*. Taken together, the above analysis suggested the advantages of hydrogel MSs culture system in maintaining stem cell self-renewal and differentiation at transcriptional level.

Although the micro-scale cell aggregates can fill up the irregular shape of the defect site, the endogenous bone regeneration may be hindered by the lack of enough vascularization and their terminal cell apoptosis, as well as the low-scaling production regarding large-sized bone defects [18]. The assembly of callus-like organoids by 3D printing into more complex structures and the subsequent chondrogenic differentiation at a certain stage were thus preferred for full bone regeneration. For instance, the channels among MSs can promote blood vessel and nerve ingrowth, important steps at the late stages of endochondral ossification when applied *in vivo* [44,45]. In the present work, rapid vascularization and ectopic bone formation can be observed after implantation, possibly owing to the space among the micro-organoids and more arranged blood vessel formation can be achieved by orderly assembly of organoids [46]. More importantly, the implantation of osteo-callus organoids formed by chondrogenic induction led to efficient in situ bone regeneration within 4 weeks in a large bone defect. In both cases, new bone formation after the implantation of pre-differentiated osteo-callus organoids exhibited a temporal-forward phase which stepped over the beginning phase of chondrogenesis that initiated in natural bone healing.

However, as native callus formation is far more complicated and many bioactive molecules, such as VEGF [47] and bone morphogenetic proteins (BMPs) [48,49], are involved in this process [9,21,47,50,51], more sophisticated design of osteo-callus organoids is still needed. The osteo-callus organoids in this study could also be utilized as bioinks for second bioprinting to construct anatomy-mimic grafts. Owing to the flexibility of bioinks in 3D printing, the pre-differentiation strategy in this study could be improved in combination with bioactive molecules to further promote precise and efficient bone regeneration. Besides, more accurate delivery system is needed to support the sequential release of these growth factors [52]. One solution is the utilization of composite materials with different degradation rate. Differentially biodegradable

materials can be used as the basic ink to encapsulate different growth factors and progenitor cells to recapitulate the various stages of callus formation. Moreover, there are still improvements needed for clinical use. Mass production of cell-loaded MSs by 3D printing is the essential requirement for a therapy. Millions of MSs will be needed for a therapeutic use when meeting large defects. Hence, improvements in 3D printing technique would help to solve the production problem. Volumetric bioprinting has provided an option to realize cell-loaded constructs in seconds with exceptionally high cell viability and has been proved to fabricate bone-like tissues [53]. Besides, dynamic MS culture systems support cell growth and differentiation. Perfusion bioreactors have been proved as an optimal platform to enhance the transport of culture medium throughout the cell-loaded constructs with dynamic forces [54] and provided possibilities to support mass MSs culture for clinical use.

5. Conclusion

In summary, this study proposes a MSs-based 3D culture system with outstanding capacity for *in vitro* chondrogenic differentiation of MSCs before the implantation, and provides a more authentic cell induction carrier platform when adopting the pre-differentiation strategy that mimics endochondral ossification for more efficient bone regeneration. Remarkably, a simultaneous state of stem cell proliferation and differentiation at transcriptional level, which highly recapitulates the diverse mesenchymal stem cell compositions and behaviors involved in endochondral ossification, has been achieved by the stem cell-incorporated 3D printing culture system. The callus-like organoids that formed by further chondrogenic differentiation showed high *in vivo* biocompatibility and vascularization. After in-situ implantation, rapid bone repair in rabbits was achieved within 4 weeks by advancing the regenerative process of endochondral ossification, which is much shorter than conventional healing time of bone defects.

Credit author statement

Chang Xie: Conceptualization, Methodology, Investigation, Visualization, Writing – original draft **Hongwei Ouyang**: Conceptualization, Supervision, Writing – original draft, Funding acquisition, **Xianzhu Zhang**: Conceptualization, Supervision, Writing – original draft, Methodology, **Renjie Liang**: Methodology, Investigation, Visualization, Writing – review & editing, **Jinchun Ye**: Methodology, Visualization, Writing – review & editing, **Zhi Peng**: Methodology, Visualization, **Heng Sun**: Methodology, Resources, **Qiuwen Zhu**: Methodology, **Xilin Shen**: Methodology, Visualization, **Yi Hong**: Methodology, Supervision, Resources, **Hongwei Wu**: Methodology, **Wei Sun**: Methodology, **Xudong Yao**: Writing – review & editing, **Jiajin Li**: Methodology, **Shufang Zhang**: Methodology

Statistical analysis

All experiments were performed with at least three replicates. The results were all represented as mean ± SD. p value lower than 0.05 (*$p < 0.5$, **$p < 0.05$, ***$p < 0.01$, ****$p < 0.0001$) was considered to be statistically significant. Data were analyzed by GraphPad Prism 8 (GraphPad Software, Inc, USA) using one-way ANOVA.

Declaration of competing interest

The authors declare that they have no known competing financial interests or personal relationships that could have appeared to influence the work reported in this paper.

Data availability

Data will be made available on request.

Acknowledgements

The authors acknowledged the financial support from the National Key Research and Development Program of China (2017YFA0104900), and NSFC grants (T2121004, 31830029). The authors thank Mrs. Shuangshuang Liu (Core Facilities, Zhejiang University School of Medicine) for her assistance with Confocal laser scanning microscope. We also thank Mrs. Beibei Wang for her helping us in transmission electron microscope.

Appendix A. Supplementary data

Supplementary data to this article can be found online at https://doi.org/10.1016/j.biomaterials.2022.121741.

References

[1] Z. Lin, Y. Zhao, P.K. Chu, L. Wang, H. Pan, Y. Zheng, S. Wu, X. Liu, K.M.C. Cheung, T. Wong, K.W.K. Yeung, A functionalized TiO2/Mg2TiO4 nano-layer on biodegradable magnesium implant enables superior bone-implant integration and bacterial disinfection, Biomaterials 219 (2019), 119372, https://doi.org/10.1016/j.biomaterials.2019.119372.
[2] B. Xu, P. Zheng, F. Gao, W. Wang, H. Zhang, X. Zhang, X. Feng, W. Liu, A mineralized high strength and tough hydrogel for skull bone regeneration, Adv. Funct. Mater. 27 (2017), https://doi.org/10.1002/adfm.201604327.
[3] P. Cheng, P. Han, C. Zhao, S. Zhang, H. Wu, J. Ni, P. Hou, Y. Zhang, J. Liu, H. Xu, S. Liu, X. Zhang, Y. Zheng, Y. Chai, High-purity magnesium interference screws promote fibrocartilaginous entheses regeneration in the anterior cruciate ligament reconstruction rabbit model via accumulation of BMP-2 and VEGF, Biomaterials 81 (2016) 14–26, https://doi.org/10.1016/j.biomaterials.2015.12.005.
[4] G.C. Ingavle, M. Gionet-Gonzales, C.E. Vorwald, L.K. Bohannon, K. Clark, L. D. Galuppo, J.K. Leach, Injectable mineralized microsphere-loaded composite hydrogels for bone repair in a sheep bone defect model, Biomaterials 197 (2019) 119–128, https://doi.org/10.1016/j.biomaterials.2019.01.005.
[5] P. Lenas, M. Moos, F.P. Luyten, Developmental engineering: a new paradigm for the design and manufacturing of cell-based products. Part I: from three-dimensional cell growth to biomimetics of in Vivo development, Tissue Eng. B Rev. 15 (2009) 381–394, https://doi.org/10.1089/ten.teb.2008.0575.
[6] J. Bernhard, J. Ferguson, B. Rieder, P. Heimel, T. Nau, S. Tangl, H. Redl, G. Vunjak-Novakovic, Tissue-engineered hypertrophic chondrocyte grafts enhanced long bone repair, Biomaterials 139 (2017) 202–212, https://doi.org/10.1016/j.biomaterials.2017.05.045.
[7] A.M. McDermott, S. Herberg, D.E. Mason, J.M. Collins, H.B. Pearson, J. H. Dawahare, R. Tang, A.N. Patwa, M.W. Grinstaff, D.J. Kelly, E. Alsberg, J. D. Boerckel, Recapitulating bone development through engineered mesenchymal condensations and mechanical cues for tissue regeneration, Sci. Transl. Med. 11 (2019) 1–16, https://doi.org/10.1126/scitranslmed.aav7756.
[8] T. Ahmad, H. Byun, J. Lee, S.K. Madhurakat Perikamana, Y.M. Shin, E.M. Kim, H. Shin, Stem cell spheroids incorporating fibers coated with adenosine and polyopamine as a modular building blocks for bone tissue engineering, Biomaterials (2020) 230, https://doi.org/10.1016/j.biomaterials.2019.119652.
[9] J. Lee, S. Lee, T. Ahmad, S.K. Madhurakkat Perikamana, J. Lee, E.M. Kim, H. Shin, Human adipose-derived stem cell spheroids incorporating platelet-derived growth factor (PDGF) and bio-minerals for vascularized bone tissue engineering, Biomaterials 255 (2020), https://doi.org/10.1016/j.biomaterials.2020.120192.
[10] Y. Li, M.D. Hoffman, D.S.W. Benoit, Matrix metalloproteinase (MMP)-degradable tissue engineered periosteum coordinates allograft healing via early stage recruitment and support of host neurovasculature, Biomaterials 268 (2021), 120535, https://doi.org/10.1016/j.biomaterials.2020.120535.
[11] G. Nilsson Hall, L.F. Mendes, C. Gklava, L. Geris, F.P. Luyten, I. Papantoniou, Developmentally engineered callus organoid bioassemblies exhibit predictive in vivo long bone healing, Adv. Sci. 7 (2020) 1–16, https://doi.org/10.1002/advs.201902295.
[12] Y. Liu, B. Kuang, B.B. Rothrau, R.S. Tuan, H. Lin, Biomaterials Robust Bone Regeneration through Endochondral Ossi Fi Cation of Human Mesenchymal Stem Cells within Their Own Extracellular Matrix, 2019, p. 218, https://doi.org/10.1016/j.biomaterials.2019.119336.
[13] H.M. Kronenberg, 4 Kronenberg, 2003, p. 423. www.nature.com/nature.
[14] K.E. Boonekamp, K. Kretzschmar, D.J. Wiener, P. Asra, S. Derakhshan, J. Puschhof, C. López-Iglesias, P.J. Peters, O. Basak, H. Clevers, Long-term expansion and differentiation of adult murine epidermal stem cells in 3D organoid cultures, Proc. Natl. Acad. Sci. U.S.A. 116 (2019) 14630–14638, https://doi.org/10.1073/pnas.1715272116.
[15] J. Andersen, O. Revah, Y. Miura, N. Thom, N.D. Amin, K.W. Kelley, M. Singh, X. Chen, M.V. Thete, E.M. Walczak, H. Vogel, H.C. Fan, S.P. Paşca, Generation of functional human 3D cortico-motor assembloids, Cell 183 (2020) 1913–1929, https://doi.org/10.1016/j.cell.2020.11.017, e26.
[16] E. Kim, S. Choi, B. Kang, J.H. Kong, Y. Kim, W.H. Yoon, H.R. Lee, S.E. Kim, H. M. Kim, H.S. Lee, C. Yang, Y.J. Lee, M. Kang, T.Y. Roh, S. Jung, S. Kim, J.H. Ku, K. Shin, Creation of bladder assembloids mimicking tissue regeneration and cancer, Nature 588 (2020) 664–669, https://doi.org/10.1038/s41586-020-3034-x.

[17] H.H.N. Yan, H.C. Siu, S.L. Ho, S.S.K. Yue, Y. Gao, W.Y. Tsui, D. Chan, A.S. Chan, J. W.H. Wong, A.H.Y. Man, B.C.H. Lee, A.S.Y. Chan, A.K.W. Chan, H.S. Hui, A.K. L. Cheung, W.L. Law, O.S.H. Lo, S.T. Yuen, H. Clevers, S.Y. Leung, Organoid cultures of early-onset colorectal cancers reveal distinct and rare genetic profiles, Gut 69 (2020) 2165–2179, https://doi.org/10.1136/gutjnl-2019-320019.
[18] Y. Qiao, Z. Xu, Y. Yu, S. Hou, J. Geng, T. Xiao, Biomaterials Single cell derived spheres of umbilical cord mesenchymal stem cells enhance cell stemness properties , survival ability and therapeutic potential on liver failure, Biomaterials 227 (2020), 119573, https://doi.org/10.1016/j.biomaterials.2019.119573.
[19] J.A. Brassard, M. Nikolaev, T. Hübscher, M. Hofer, M.P. Lutolf, Recapitulating macro-scale tissue self-organization through organoid bioprinting, Nat. Mater. 20 (2021) 22–29, https://doi.org/10.1038/s41563-020-00803-5.
[20] M.E. Kupfer, W.H. Lin, V. Ravikumar, K. Qiu, L. Wang, L. Gao, D.B. Bhuiyan, M. Lenz, J. Ai, R.R. Mahutga, D.W. Townsend, J. Zhang, M.C. McAlpine, E. G. Tolkacheva, B.M. Ogle, In Situ Expansion, Differentiation, and Electromechanical Coupling of Human Cardiac Muscle in a 3D Bioprinted, Chambered Organoid, Circ. Res., 2020, pp. 207–224, https://doi.org/10.1161/CIRCRESAHA.119.316155.
[21] S. Yamano, K. Haku, T. Yamanaka, J. Dai, T. Takayama, R. Shohara, K. Tachi, M. Ishioka, S. Hanatani, S. Karunagaran, K. Wada, A.M. Moursi, The effect of a bioactive collagen membrane releasing PDGF or GDF-5 on bone regeneration, Biomaterials 35 (2014) 2446–2453, https://doi.org/10.1016/j.biomaterials.2013.12.006.
[22] S. Lück, R. Schubel, J. Rüb, D. Hahn, E. Mathieu, H. Zimmermann, D. Scharnweber, C. Werner, S. Pautot, R. Jordan, Tailored and biodegradable poly(2-oxazoline) microbeads as 3D matrices for stem cell culture in regenerative therapies, Biomaterials 79 (2016) 1–14, https://doi.org/10.1016/j.biomaterials.2015.11.045.
[23] C. Yu, A. Kornmuller, C. Brown, T. Hoare, L.E. Flynn, Decellularized adipose tissue microcarriers as a dynamic culture platform for human adipose-derived stem/stromal cell expansion, Biomaterials 120 (2017) 66–80, https://doi.org/10.1016/j.biomaterials.2016.12.017.
[24] E.L.H. Daley, R.M. Coleman, J.P. Stegemann, Biomimetic microbeads containing a chondroitin sulfate/chitosan polyelectrolyte complex for cell-based cartilage therapy, J. Mater. Chem. B. 3 (2015) 7920–7929, https://doi.org/10.1039/c5tb00934k.
[25] Y. Wang, X. Yuan, K. Yu, H. Meng, Y. Zheng, J. Peng, S. Lu, X. Liu, Y. Xie, K. Qiao, Fabrication of nanofibrous microcarriers mimicking extracellular matrix for functional microtissue formation and cartilage regeneration, Biomaterials 171 (2018) 118–132, https://doi.org/10.1016/j.biomaterials.2018.04.033.
[26] R.T. Annamalai, X. Hong, N.G. Schott, G. Tiruchinapally, B. Levi, J.P. Stegemann, Injectable osteogenic microtissues containing mesenchymal stromal cells conformally fill and repair critical-size defects, Biomaterials 208 (2019) 32–44, https://doi.org/10.1016/j.biomaterials.2019.04.001.
[27] X. Zhao, S. Liu, L. Yildirimer, H. Zhao, R. Ding, H. Wang, W. Cui, D. Weitz, Injectable stem cell-laden photocrosslinkable microspheres fabricated using microfluidics for rapid generation of osteogenic tissue constructs, Adv. Funct. Mater. 26 (2016) 2809–2819, https://doi.org/10.1002/adfm.201504943.
[28] D.X. Wei, J.W. Dao, G.Q. Chen, A micro-ark for cells: highly open porous polyhydroxyalkanoate microspheres as injectable scaffolds for tissue regeneration, Adv. Mater. 30 (2018) 1–10, https://doi.org/10.1002/adma.201802273.
[29] Q. He, Y. Liao, J. Zhang, X. Yao, W. Zhou, Y. Hong, H. Ouyang, All-in-One" gel system for whole procedure of stem-cell amplification and tissue engineering, Small 16 (2020) 1–9, https://doi.org/10.1002/smll.201906539.
[30] S. Xiao, T. Zhao, J. Wang, C. Wang, J. Du, L. Ying, J. Lin, C. Zhang, W. Hu, L. Wang, K. Xu, Gelatin methacrylate (GelMA)-Based hydrogels for cell transplantation: an effective strategy for tissue engineering, Stem Cell Rev. Reports 15 (2019) 664–679, https://doi.org/10.1007/s12015-019-09893-4.
[31] Y. Hong, F. Zhou, Y. Hua, X. Zhang, C. Ni, D. Pan, Y. Zhang, D. Jiang, L. Yang, Q. Lin, Y. Zou, D. Yu, D.E. Arnot, X. Zou, L. Zhu, S. Zhang, H. Ouyang, A strongly adhesive hemostatic hydrogel for the repair of arterial and heart bleeds, Nat. Commun. 10 (2019) 1–11, https://doi.org/10.1038/s41467-019-10004-7.
[32] Y. Yang, J. Zhang, Z. Liu, Q. Lin, X. Liu, C. Bao, Y. Wang, L. Zhu, Tissue-integratable and biocompatible photogelation by the imine crosslinking reaction, Adv. Mater. 28 (2016) 2724–2730, https://doi.org/10.1002/adma.201505336.
[33] A. Dobin, C.A. Davis, F. Schlesinger, J. Drenkow, C. Zaleski, S. Jha, P. Batut, M. Chaisson, T.R. Gingeras, STAR: ultrafast universal RNA-seq aligner, Bioinformatics 29 (2013) 15–21, https://doi.org/10.1093/bioinformatics/bts635.
[34] F. Zhou, Y. Hong, R. Liang, X. Zhang, Y. Liao, D. Jiang, J. Zhang, Z. Sheng, C. Xie, Z. Peng, X. Zhuang, V. Bunpetch, Y. Zou, W. Huang, Q. Zhang, E.V. Alakpa, S. Zhang, H. Ouyang, Rapid printing of bio-inspired 3D tissue constructs for skin regeneration, Biomaterials 258 (2020), 120287, https://doi.org/10.1016/j.biomaterials.2020.120287.
[35] E.J. Mackie, Y.A. Ahmed, L. Tatarczuch, K.S. Chen, M. Mirams, Endochondral ossification: how cartilage is converted into bone in the developing skeleton, Int. J. Biochem. Cell Biol. 40 (2008) 46–62, https://doi.org/10.1016/j.biocel.2007.06.009.
[36] J. Sherwood, J. Bertrand, G. Nalesso, B. Poulet, A. Pitsillides, L. Brandolini, A. Karystinou, C. De Bari, F.P. Luyten, C. Pitzalis, T. Pap, F. Dell'Accio, A homeostatic function of CXCR2 signalling in articular cartilage, Ann. Rheum. Dis. 74 (2015) 2207–2215, https://doi.org/10.1136/annrheumdis-2014-205546.
[37] N. Ono, W. Ono, T. Nagasawa, H.M. Kronenberg, A subset of chondrogenic cells provides early mesenchymal progenitors in growing bones, Nat. Cell Biol. 16 (2014) 1157–1167, https://doi.org/10.1038/ncb3067.
[38] S. Egawa, S. Miura, H. Yokoyama, T. Endo, K. Tamura, Growth and differentiation of a long bone in limb development, repair and regeneration, Dev. Growth Differ. 56 (2014) 410–424, https://doi.org/10.1111/dgd.12136.
[39] D. Aran, A.P. Looney, L. Liu, E. Wu, V. Fong, A. Hsu, S. Chak, R.P. Naikawadi, P. J. Wolters, A.R. Abate, A.J. Butte, M. Bhattacharya, Reference-based analysis of lung single-cell sequencing reveals a transitional profibrotic macrophage, Nat. Immunol. 20 (2019) 163–172, https://doi.org/10.1038/s41590-018-0276-y.
[40] T. Long, Z. Zhu, H.A. Awad, E.M. Schwarz, M.J. Hilton, Y. Dong, The effect of mesenchymal stem cell sheets on structural allograft healing of critical sized femoral defects in mice, Biomaterials 35 (2014) 2752–2759, https://doi.org/10.1016/j.biomaterials.2013.12.039.
[41] T. Wang, Y. Zhai, M. Nuzzo, X. Yang, Y. Yang, X. Zhang, Layer-by-layer nanofiber-enabled engineering of biomimetic periosteum for bone repair and reconstruction, Biomaterials 182 (2018) 279–288, https://doi.org/10.1016/j.biomaterials.2018.08.028.
[42] J. Guerrero, S. Pigeot, J. Müller, D.J. Schaefer, I. Martin, A. Scherberich, Fractionated human adipose tissue as a native biomaterial for the generation of a bone organ by endochondral ossification, Acta Biomater. 77 (2018) 142–154, https://doi.org/10.1016/j.actbio.2018.07.004.
[43] L. Sun, Y. Ma, H. Niu, Y. Liu, Y. Yuan, C. Liu, Recapitulation of in situ endochondral ossification using an injectable hypoxia-mimetic hydrogel, Adv. Funct. Mater. 31 (2021) 1–19, https://doi.org/10.1002/adfm.202008515.
[44] M. Zhang, R. Lin, X. Wang, J. Xue, C. Deng, C. Feng, H. Zhuang, J. Ma, C. Qin, L. Wan, J. Chang, C. Wu, 3D printing of Haversian bone-mimicking scaffolds for multicellular delivery in bone regeneration, Sci. Adv. 6 (2020), https://doi.org/10.1126/sciadv.aaz6725.
[45] W. Zhang, C. Feng, G. Yang, G. Li, X. Ding, S. Wang, Y. Dou, Z. Zhang, J. Chang, C. Wu, X. Jiang, 3D-printed scaffolds with synergistic effect of hollow-pipe structure and bioactive ions for vascularized bone regeneration, Biomaterials 135 (2017) 85–95, https://doi.org/10.1016/j.biomaterials.2017.05.005.
[46] A.C. Daly, M.D. Davidson, J.A. Burdick, 3D bioprinting of high cell-density heterogeneous tissue models through spheroid fusion within self-healing hydrogels, Nat. Commun. 12 (2021) 1–13, https://doi.org/10.1038/s41467-021-21029-2.
[47] M. Keeney, J.J.J.P. van den Beucken, P.M. van der Kraan, J.A. Jansen, A. Pandit, The ability of a collagen/calcium phosphate scaffold to act as its own vector for gene delivery and to promote bone formation via transfection with VEGF165, Biomaterials 31 (2010) 2893–2902, https://doi.org/10.1016/j.biomaterials.2009.12.041.
[48] H. Niu, Y. Ma, G. Wu, B. Duan, Y. Wang, Y. Yuan, C. Liu, Multicellularity-interweaved bone regeneration of BMP-2-loaded scaffold with orchestrated kinetics of resorption and osteogenesis, Biomaterials 216 (2019), 119216, https://doi.org/10.1016/j.biomaterials.2019.05.027.
[49] D.B. Raina, I. Qayoom, D. Larsson, M.H. Zheng, A. Kumar, H. Isaksson, L. Lidgren, M. Tägil, Guided tissue engineering for healing of cancellous and cortical bone using a combination of biomaterial based scaffolding and local bone active molecule delivery, Biomaterials 188 (2019) 38–49, https://doi.org/10.1016/j.biomaterials.2018.10.004.
[50] Y. Zhang, N. Cheng, R. Miron, B. Shi, X. Cheng, Delivery of PDGF-B and BMP-7 by mesoporous bioglass/silk fibrin scaffolds for the repair of osteoporotic defects, Biomaterials 33 (2012) 6698–6708, https://doi.org/10.1016/j.biomaterials.2012.06.021.
[51] E. Quinlan, S. Partap, M.M. Azevedo, G. Jell, M.M. Stevens, F.J. O'Brien, Hypoxia-mimicking bioactive glass/collagen glycosaminoglycan composite scaffolds to enhance angiogenesis and bone repair, Biomaterials 52 (2015) 358–366, https://doi.org/10.1016/j.biomaterials.2015.02.006.
[52] S. Uchida, A. Sakai, H. Kudo, H. Otomo, M. Watanuki, M. Tanaka, M. Nagashima, T. Nakamura, Vascular endothelial growth factor is expressed along with its receptors during the healing process of bone and bone marrow after drill-hole injury in rats, Bone 32 (2003) 491–501, https://doi.org/10.1016/S8756-3282(03)00053-X.
[53] J. Gehlen, W. Qiu, G.N. Schädli, R. Müller, X.-H. Qin, Tomographic volumetric bioprinting of heterocellular bone-like tissues in seconds, Acta Biomater. (2022), https://doi.org/10.1016/j.actbio.2022.06.020.
[54] D.P. Forrestal, M.C. Allenby, B. Simpson, T.J. Klein, M.A. Woodruff, Personalized volumetric tissue generation by enhancing multiscale mass transport through 3D printed scaffolds in perfused bioreactors, Adv. Healthc. Mater. 2200454 (2022), e2200454, https://doi.org/10.1002/adhm.202200454.